[Title page]

1. Title: Turbulent flame propagation of polymethylmethacrylate particle clouds in an O_2/N_2 atmosphere

2. Author(s): Yu Xia [a], Nozomu Hashimoto [a,*], Osamu Fujita [a]

[a] *Division of Mechanical and Space Engineering, Hokkaido University,*

Kita13 Nishi8, Kita-ku, Sapporo 060-8628, Japan

3. Corresponding author information:

Nozomu Hashimoto*

Professor, Hokkaido University,

Kita13 Nishi8, Kita-ku, Sapporo 060-8628, Japan

E-mail address: nozomu.hashimoto@eng.hokudai.ac.jp

Tel.: +81-11-706-6386

Fax: +81-11-706-7841

Abstract:

The combustion of solid particle clouds is extensively used in many engineering areas. However, experimental data describing the turbulent flame propagation behavior and the combustion mechanism of solid particle clouds have remained limited. In this work, the combustion of polymethylmethacrylate (PMMA) particle clouds was studied by employing a unique fan-stirred constant-volume chamber. For the quasi-monodispersed particle clouds, the flame propagation velocity increased with the increase in the turbulence intensity and the decrease in the quasi-monodispersed particle size. However, the particle concentration had little effect on the flame propagation velocity, which is unique in a turbulent flow field. The consistency of the results between the current study of PMMA particle clouds and the previous study for coal particle clouds showed that the heterogeneous combustion of char particles had little effect on the turbulent flame propagation velocity of the solid particle clouds. Further, two types of quasi-monodispersed particles were mixed to study how the interactions between small and large (polydispersed) particles affect turbulent flame propagation. We found that the turbulent flame propagation velocity had a nonlinear relationship with the mass ratio of small particles (J-shaped curve). The turbulent flame propagation velocity slightly increased with low mass ratio of small particles, while it sharply increased with high mass ratio of small particles. Increasing the turbulence intensity and decreasing the primary particle (large particle) size can advance the starting point of the sharp increase. These unique features were explained by a mechanism considering the polydispersed interparticle interaction proposed by the authors. In the combustion of turbulent polydispersed particle clouds, the particle–particle agglomeration and the agglomeration break-up in the turbulent flow field affect turbulent flame propagation. To the best of our knowledge, this is the first report on the fundamental spherical turbulent flame propagation phenomenon and the mechanism of solid particle cloud combustion considering the polydispersed interparticle interactions.

Keywords: Solid particle cloud turbulent combustion; Turbulent flame propagation; Particle size effect; particle-particle interaction; PMMA particle

* Corresponding author: Tel.: +81-11-706-6386. E-mail address: nozomu.hashimoto@eng.hokudai.ac.jp

1. Introduction

The combustion of solid particle clouds, such as pulverized coal, biomass, and metal, has been extensively used in many engineering areas, such as energy generation and propulsion systems. The combustion characteristics of solid particle clouds have been studied under a laminar condition, such as flame structure [1], flame propagation speed [2–7], flammability limit [8–10], and quenching distance [11,12]. From a practical perspective, almost all the combustion of solid particle clouds is utilized under a turbulent environment. However, studies concerning the combustion of the turbulent solid particle cloud have remained limited, and the basic turbulent combustion mechanism of solid particle clouds is yet to be understood. Three major problems exist regarding the turbulent combustion of solid particle clouds [13]. The first one is the complexity of the combustion process. Under particle cloud combustion, the particles undergo the process of heat-up, pyrosis or devolatilization, mixing with an oxidizer, ignition and combustion. Second, interactions between particles differ due to particle size, shape, size distribution, and fuel type. Third, if the solid particle combustion occurs in a turbulent environment, turbulence affects heat and mass transfer and flame shape [14,15]. Besides, turbulence can accelerate particle motion to enhance particle–particle interactions. Consequently, the combustion process of solid particle clouds in the turbulent environment is complicated.

Therefore, a few studies have been conducted to investigate on the combustion of solid particle clouds in the turbulent environment, such as minimum ignition energy (MIE) [16,17], pressure [18], and particle burning time [19]. Because the combustion of solid particle clouds is affected by the physical and chemical properties of the particles and combustion circumstances such as the oxidizer concentration, gravitation and atmospheric temperature, the flame propagation velocity becomes important to characterize the combustion of solid particle clouds. In coal-fired boilers, it is used to characterize the stability of the flame, which is an important property for the burner. Kauffman et al. and Pu et al. [20–22] reported the quantitative effect of turbulence on the premixed dust/air flame under various turbulence intensities and

particle sizes and concentrations through the dispersion-induced nonstationary turbulence method. Schneider et al. [23] reported the relationship between the turbulent burning velocity and the turbulence intensity by the open-tube method with the dispersion-induced turbulence. Most recently, Zhang et al. [24] studied the turbulent intensity effect on the nano-PMMA flame propagation behavior by the dispersion-induced turbulence method. To sustain the uniform turbulence intensity during solid particle combustion, Hadi et al. [14,15,25–28] developed a unique turbulence combustion apparatus for solid particle clouds. The near-homogeneous turbulence and uniform dispersion can be obtained using their combustion apparatus. They found that the turbulent heat and mass transfer is the dominant factor for affecting turbulent flame propagation, and the particle cloud concentration weakly affects the flame propagation velocity. However, turbulent flame propagation was achieved using polydispersed coal particle clouds under a constant average size. In the combustion of polydispersed particle clouds, some interactions between small and large particles affect the turbulent flame propagation [29]. Moreover, particles of different fuel materials have different combustion behaviors. Therefore, it is important to validate previous conclusions using different quasi-monodispersed solid particle clouds of fuel materials and investigate their turbulent flame propagation mechanism.

Further, the fundamental turbulent flame propagation mechanism has not been clarified for different quasi-monodispersed particle sizes, and polydispersed particle clouds associating with small–large particle's interactions. As defined in the laminar condition, the particle size strongly affects flame propagation due to the vast change in the specific surface area [6]. However, the quasi-monodispersed particle size effect on flame propagation in the near-homogeneous turbulent flow field has not been studied. From a practical perspective, almost all particle clouds have polydispersed characteristics. In the combustion of polydispersed particle clouds in a laminar condition, the particle size distribution is a critical factor for determining the flame propagation mechanism [13,30–32]. However, effects of the

interparticle interactions on the combustion of polydispersed particle clouds in the turbulent flow field have yet to be studied.

To eliminate the effect of heterogeneous char combustion on the solid particle cloud turbulent flame propagation and to simplify the solid particle cloud turbulent combustion, the polymethylmethacrylate (PMMA) solid particles were experimentally used as i) the molecular structure and physical properties of PMMA particles are well-known; ii) PMMA particles are quasi-monodispersed, and the particle size distribution can be easily controlled and measured [4]; iii) PMMA particle can be "cleanly" devolatilized at elevated temperature, decomposing to its gaseous monomer, methyl methacrylate (MMA) [33]; iv) no solid residue or char remains to complicate the heat transfer problem, i.e., no heterogeneous combustion mode exists, such as char combustion.

Therefore, we aimed to clarify the behavior and fundamental mechanism of the turbulent flame propagation of solid quasi-monodispersed particle clouds under various particle concentrations and sizes. Further, particles with different sizes were mixed to study the turbulent flame propagation of the polydispersed particle clouds by considering the effects of interparticle interactions. Based on the results obtained from the study, new models of the turbulent combustion numerical simulation of solid particle clouds can be developed in the future.

2. Experimental apparatus and methods

2.1. Experimental setup

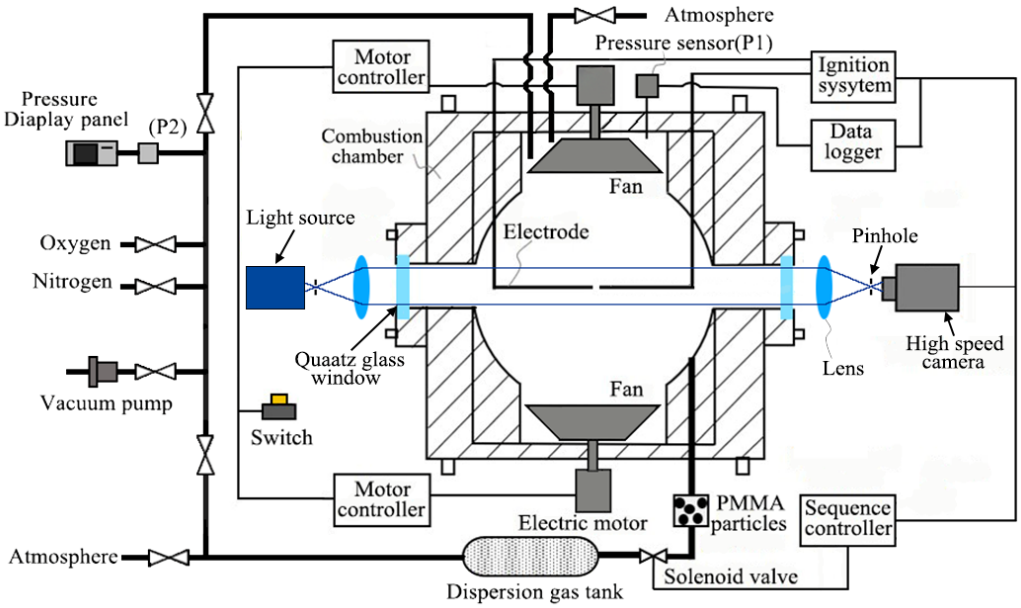

Fig. 1 Schematic of the experimental setup.

The experimental apparatus is depicted in Fig. 1. PMMA particle cloud combustion experiments were conducted using a constant-volume spherical chamber with an inside diameter of 200 mm and a height of 280 mm. The total volume of the chamber was 6.19×10^{-3} m^3. Four 50-mm-diameter quartz glass windows were installed to observe flame propagation in the chamber. These optical windows were mounted opposite to each other.

A capacitor discharge ignition circuit system was adapted to ignite the particle clouds/oxidizer mixture [14,25]. The ignition energy was set as 5.5 J, which was the same as previously used for the combustion of solid particle clouds [14,15,27]. To facilitate the observation of the combustion, the electrodes were mounted at a 45º angle with respect to the interrogation path.

Turbulence was generated by two identical counter-rotation seven-bladed fans mounted vertically and symmetrically at the top and bottom of the chamber. Each fan, which was rotated by directly coupled electric motors (Maxon Motor, RE50) with separate speed controllers (Maxon Motor, ESCON 50/5), can be precisely adjustable between 0 and 15,000 rpm. The fan rotation speed error was within ±1 rpm. Turbulence characteristics were measured by particle image velocimetry (PIV) (explained in the

Appendix—PIV measurement [14,25]). As a result of the PIV measurement, the turbulence was found to be isotropic and homogeneous, and there was almost no regular bulk motion. Turbulence intensity, u', which was proportional to the fan speed, f_s, was found to be represented by Eq. (1) [14,25,26],

$$u' = 0.00129 f_s, \tag{1}$$

where f_s is the fan speed in rpm. The longitudinal integral length scale, L_f, determined by two-point correlation, was 20.9 mm regardless of the turbulence intensity [14].

Three types of photography were used to capture the flame propagation: direct imaging, OH radical photography, and schlieren photography. The detailed setting of the three photography can be seen in Fig. AA in Appendix. In our previous studies involving pure pulverized coal particle cloud combustion and pulverized coal particle cloud/ammonia co-combustion, schlieren photography was not used because of the strong light scattering of polydispersed particles. Interestingly, in the PMMA particle cloud combustion experiments, schlieren photography could be used to capture flame propagation. Details of direct imaging, schlieren photography, and OH photography were explained in our previous studies [15,25–27]. The frame rates of high-speed cameras for direct imaging, schlieren photography, and OH photography were set at 2500–3500 fps. The resolution for the cameras were 512 × 512, 512 × 512 and 400 × 400, respectively. Notably, direct imaging was used as a reference for the combustion phenomenon. The flame propagation image, which was obtained by direct imaging, was not analyzed since it was hard to define the border of the flame front due to the weak intensity of soot formation in the flame propagation process.

2.2. Particle properties

Quasi-monodispersed PMMA particles with diameters of 3, 10, 20, and 30 μm [34] were used. The PMMA particle clouds had a narrow particle size distribution. Figure 2 shows the micrographs of the PMMA particles obtained by scanning electron microscopy (SEM, JSM-7001FA). Additionally, the size distribution of the particles was almost uniform (see Table AA, AB, AC, and AD and Fig. AB, AC, AD, and AE in Appendix). The characteristic particle parameters can be seen in Table AE in Appendix. As shown in Fig. 2, the spherical PMMA particles had a narrow particle size distribution, which could be treated as quasi-monodispersed particles.

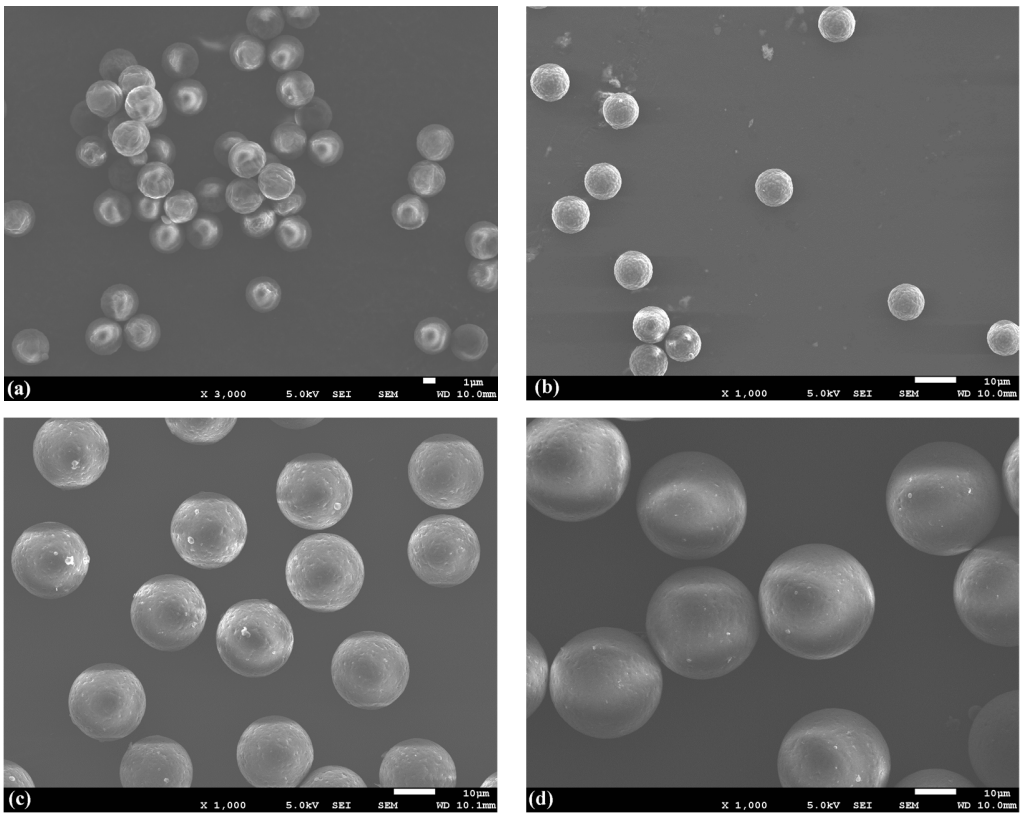

Fig. 2 Scanning electron microscopy (SEM) micrographs of the quasi-monodispersed particles: (a) 3-μm particles, (b) 10-μm particles, (c) 20-μm particles, and (d) 30-μm particles.

2.3. Experimental conditions

In this work, the particle concentration effect was studied by changing the PMMA particles concentration from 0.6 kg/m^3 to 2.3 kg/m^3 for the quasi-monodispersed particles with a diameter of 30-μm. To reveal the particle size effect, three types of quasi-monodispersed particles with diameters of 10, 20, and 30 μm were used. However, for the 10-μm quasi-monodispersed particles, schlieren and OH photography cannot capture flame propagation images due to strong light scattering. Therefore, to clarify the quasi-monodispersed particle size effect on the flame propagation, the pressure histories for all conditions were recorded.

A simplified polydispersed particle cloud was made by mixing two types of quasi-monodispersed particles to clarify the interparticle interaction effect on the combustion of solid particle clouds in the turbulent environment. Three particle mixtures were prepared, including the mixture of 10-μm quasi-monodispersed particles and 30-μm quasi-monodispersed particles, 3-μm quasi-monodispersed particles and 30-μm quasi-monodispersed particles, and 10-μm quasi-mono-dispersed particles and 20-μm quasi-monodispersed particles. To ensure the repeatability of the experiments for each condition, the total mass of the particle clouds after mixing was constant at 100 g. For the mixing procedure, first, the mass of the small quasi-monodispersed particles and large quasi-monodispersed particles were measured by the electric scale (Mettler AJ150) based on the mass ratio. Subsequently, the quasi-monodispersed particles were loaded into a 1-L pillar-shaped bottle (Monotaro M1000L). Then, the bottle was shaken for about an hour.

To guarantee the reliability of the mixing method, SEM observations were conducted. As shown in Fig. 3, near-homogeneous mixing can be achieved through the mixing method. The detailed experimental conditions can be seen in Table 1.

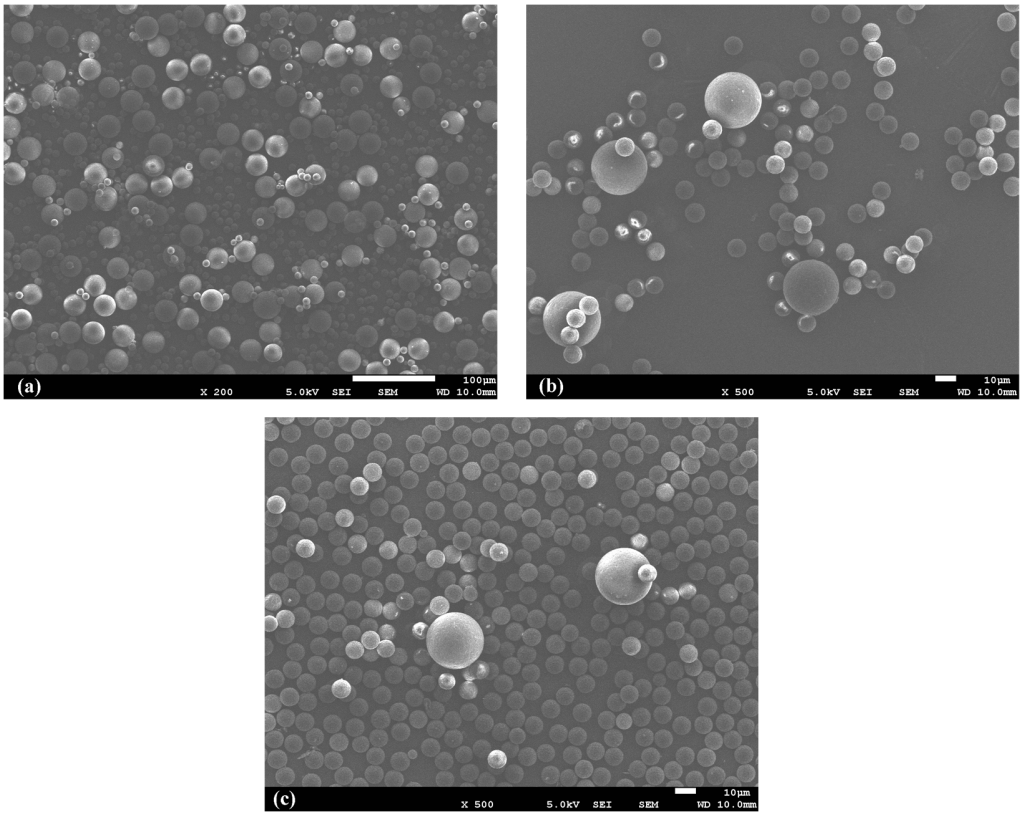

Fig. 3 SEM micrographs after mixing quasi-monodispersed particles with different diameters: (a) 80% 30-µm particles and 20% 10-µm particles; (b) 50% 30-µm particles and 50% 10-µm particles; (c) 20% 30-µm particles with 80% 10-µm particles.

Table 1
Experimental conditions

Effect to be clarified	Experimental conditions		
	Particle diameter, µm	Particle concentration, kg/m^3	Mixing ratio
Particle concentration effect	30	0.6, 1.0, 1.3, 1.6, 2.0, 2.3	-
Particle size effect	30 or 20 or 10	0.6	-
Small–large particle interaction effect (mixing quasi-monodispersed particles with different sizes)	30 + 10	0.6, 1.0, 1.3	0.1, 0.2, 0.3, 0.4, 0.5, 0.6, 0.7, 0.8, 0.9 (Mass ratio of 10 µm)
	30 + 3	0.6	0.1, 0.2(Mass ratio of 3 µm)
	20 + 10	0.6	0.1, 0.2, 0.3, 0.4 (Mass ratio of 10 µm)

2.4. Experimental procedure

As the first procedure of the experiments, the PMMA particles were equally filled into four filter cups connected to the inlets. Then, the combustion chamber and the dispersion tank were emptied to 0 kPa through a vacuum pump. Subsequently, the dispersion tank was filled with 40% O_2 and 60% N_2 at 300 kPa. Similarly, the gas mixture with the same composition was supplied into the chamber. However, the gas mixture in the chamber was set to 75 kPa to ignite the solid particle cloud/oxygen/nitrogen mixture at 101 kPa (atmosphere pressure) after dispersion. The dispersion gas swept the PMMA particles into the center of the spherical chamber within 0.7 s. 0.3 s after the dispersion ended, the mixture was ignited at atmosphere pressure [14,15,27]. The fans started to rotate for 5 min before dispersion to give the desired turbulence intensity. The initial temperature of the mixture for all experiments was constant at 293 ± 3 K. The maximum errors for the O_2 concentration, pressure, and particle concentration were 1%, 5%, and 3%, respectively. At least three experiments were conducted for each condition to ensure the reliability of the experimental data.

2.5. Particle-turbulence interaction in a homogeneous isotropic turbulence flow flied

Ammonia/air and ammonia/oxygen/nitrogen (diluted oxidizer: 40% oxygen with 60% nitrogen) mixtures were used to investigate the effect of dispersion flow on the turbulent flame propagation behavior [35]. Isolated experiments were performed on the quiescent mixtures, and mixtures with dispersion flow in the same procedure as PMMA particle combustion [35]. The dispersion flow effect on the turbulent flame radius and propagation velocity can be seen in Fig. AF and Table. AG in Appendix. Both ammonia/air and ammonia/oxygen/nitrogen mixtures showed that the dispersion flow does not influence the flame propagation behavior.

In this work, particles were dispersed into the homogeneous turbulence flow. There may have the particle-turbulence interaction effect. First, the turbulence characteristics maybe influenced by the solid particles. Second, the particle motion is affected by the turbulence.

For turbulence modulation by particles, Gore and Crowe [36] found that turbulence intensity of fluid might be increased by particles when the particle diameter is larger than $0.1L_f$, whereas it might be suppressed by particles when particle diameter smaller than $0.1L_f$, in which L_f is the integral length scale of turbulence. Although this is a purely empirical observation and a very simple expression, it is widely accepted as the best criteria for evaluating the turbulence modulation by particles [37–39]. Balachandar and Eaton [39,40] also suggested that turbulence modulation in dilute flows may be caused by (1) particles enhancing the dissipation, (2) particles transferring kinetic energy to the fluid, and (3) formation of particle wakes. Therefore, for present research, the turbulence intensity might be decreased a little by the particles' interaction because the diameter of the PMMA particle used for this work is much smaller than $0.1L_f$. However, there is currently no general model that can be used reliably to qualitatively predict carrier phase turbulence in the particle-laden flow [39,41].

Further, to understand the particle motion caused by the turbulence eddies in a homogeneous isotropic turbulence flow, the Stokes number (St) [39], which is a very important dimensionless parameter in fluid–particle flow and can be calculated by the ratio of the particle response time to the characteristic timescale of the turbulent flow, was examined for our experiments. The Stokes number related to the particle velocity is defined as Eq. (2) [39],

$$St = \frac{t_v}{t_f} \tag{2}$$

where t_f is characteristic time of the flow field. If $St \ll 1$, the response time of the particles is much less than the characteristic time associated with the flow field. Thus, the particles will have ample time to respond to changes in flow velocity. Consequently, the particle and fluid velocities will be nearly equal

(velocity equilibrium). On the other hand, if $St >> 1$, the particles will have no time to respond to the fluid velocity changes and the particle velocity will be little affected [39].

The response time of a particle or droplet to changes in flow velocity is important in establishing non-dimensional parameters to characterize the flow. The momentum response time relates to the time required for a particle or droplet to respond to a change in velocity. The momentum (velocity) response time, t_v, is estimated by Eq. (3) [39],

$$t_v = \frac{\rho_p d_p^2}{18\mu_g} \tag{3}$$

where ρ_p is the particle density, d_p is the particle diameter and μ_g is the gas dynamic viscosity. In the present study, the ambient gas was diluted oxygen (40 vol% O_2 and 60 vol% N_2). The gas dynamic viscosity was calculated using the website of the Dandy research Group at Colorado State University [42]. By taking the ρ_p as 1200 kg/m³ and μ_g as 1.5753×10^{-5} m^2/s, the particle relaxation time is estimated as 3.81 ms, 1.69 ms, and 0.4 ms for 30 μm, 20 μm, and 10 μm particles, respectively.

The characteristic time for the flow can be the longest time scale $t_{f\text{-}I} = L_f/u'$, the Taylor time scale $t_{f\text{-}T} = \lambda_f/u'$, and smallest time scale $t_{f\text{-}K} = \eta_k/u'$. L_f, λ_f, and η_k are turbulence longitudinal integral length scale, longitudinal Taylor length scale, and Kolmogorov length scale, respectively. The turbulence length scales were obtained from our previous research [25,26].

The calculation results of the Stokes number associated with turbulence longitudinal integral length scale, longitudinal Taylor length scale, and Kolmogorov length scale for quasi-monodispersed particle under various turbulence intensities can be seen in Table 2.

Table 2 The stokes number based on longitudinal integral time scale, Taylor time scale, and Kolmogorov time scale for quasi-monodispersed particle under various turbulence intensities

Stokes number	Particle size (μm)	u' = 0.32 m/s	u' = 0.65 m/s	u' = 0.97 m/s	u' = 1.29 m/s
$St_I=\frac{t_v}{t_{f\text{-}I}}=\frac{t_v u'}{L_f}$	30 μm	0.0583	0.1185	0.1768	0.2352
	20 μm	0.0259	0.0526	0.0784	0.1043
	10 μm	0.0061	0.0124	0.0186	0.0247
$St_T=\frac{t_v}{t_{f\text{-}T}}=\frac{t_v u'}{\lambda_f}$	30 μm	0.2804	0.8055	1.4722	2.2607
	20 μm	0.1090	0.4428	0.9911	1.7574
	10 μm	0.0100	0.0576	0.1579	0.3234
$St_K=\frac{t_v}{t_{f\text{-}K}}=\frac{t_v u'}{\eta_K}$	30 μm	5.2074	17.7891	35.9816	59.3748
	20 μm	2.3098	7.8907	15.9603	26.3369
	10 μm	0.5467	1.8676	3.7776	6.2336

As shown in Table 2, the particles used for present research are well following the largest scale eddies and Taylor scale eddies. However, the particles are not well following the smallest scale eddies. Under this circumstance, it was suggested by researchers in fluid mechanics that heavy particles might be swept out of intense smallest-scale eddies (Kolmogorov scale) due to centrifugal effects and accumulate along the outer peripheries of eddies [41,43–47]. Essentially, this effect is believed to potentially play an important role in enhancing the particle collision rate and eventually the agglomeration rate [45,47]. This furtherly validates the importance of consideration of agglomeration mechanism when understanding the phenomena of co-combustion of quasi-mono-dispersed particle of different sizes. However, currently, the quantification of the preferential concentration effect is still an open question to discussed in fluid mechanics and combustion filed [41].

3. Experimental results for quasi-monodispersed particle clouds and mixing different size quasi-monodispersed particles clouds

3.1. Flame observation

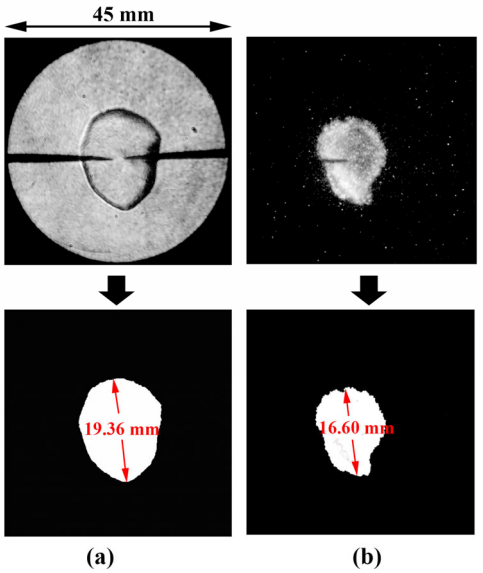

Fig. 4 Image processing; (a) Schlieren photography image; (b) OH radical photography image.

Figure 4(a) shows the schlieren image processing procedure for the combustion of 30-μm quasi-monodispersed PMMA particle clouds under a particle concentration of 0.6 kg/m^3 and a turbulence intensity of $u^{'}$ = 0.32 m/s. First, the 16-bit image was processed by gray levels from 0 = black (flame) to 255 = white (background) through applying a threshold value. Then, the processed image was transferred to the binary image in which the flame was white, and the background was black. The threshold value of the detected light intensity was selected based on visual inspection for determining the flame edge. The effects of changing the threshold value on the radius and velocity deviations were within ±2%, which was clarified in our previous research [15]. Video files of the schlieren photography are available as the Supplementary Materials (Video 1: u' = 0.32 m/s, Video 2: u' = 0.65 m/s, Video 3: u' = 0.97 m/s, Video 4: u' = 1.29 m/s. The particle concentration was 0.6 kg/m^3 and the particle diameter was 30 μm for all videos.).

Figure 4(b) shows the OH radical image for the same condition and time shown in Fig. 4(a). The border of the OH radical image was considered as the reaction front where the combustion reaction started [15]. Subsequently, the flame radii were calculated by measuring the flame tips. Even though the turbulent flame radius calculated using the flame area method and directly measuring the flame tips are different, the radius calculation method had little effect on the exact value and basic tendency of the turbulent flame propagation velocity under different turbulence intensities (the comparison of the flame radius and turbulent flame propagation velocity using two different radius calculation methods can be seen in Figs. AG and AH in Appendix).

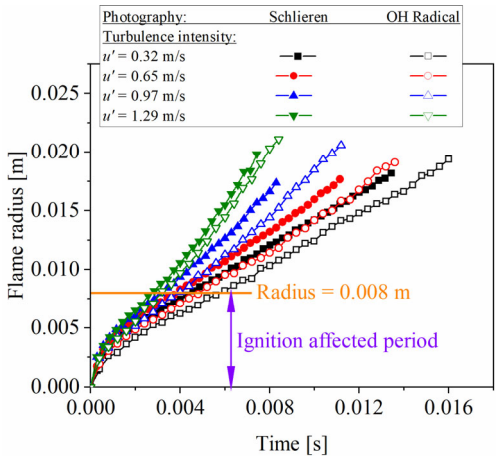

Fig. 5 Flame radius histories measured by schlieren photography and OH radical photography for the 30-μm quasi-monodispersed PMMA particles with a particle concentration of 0.6 kg/m^3.

Figure 5 shows the schlieren image flame and OH radical image flame radii histories for the combustion of the 30-μm quasi-monodispersed PMMA particle clouds at a particle concentration of 0.6 kg/m^3 with different turbulence intensities. The ignition-affected period for the flame propagation was determined in our previous research using the ammonia/oxygen/nitrogen mixture. The results showed that the radius affected by the ignition energy is within 0.008 m [26]. Therefore, to eliminate the ignition-affected period, only the flame radii data from 0.008 m to the flame front touching the window edge was used for calculating the flame propagation speed [15]. As shown in Fig. 5, the schlieren flame radius is always

larger than the OH radical flame radius at the same elapsed time under the same conditions because schlieren photography, which can capture the position of high-density gradient caused by the rapid change in gas temperature, detects the preheated zone front, while OH radical photography detects the reaction front, which follows the preheated zone, as clarified in our previous studies [15,27]. The pressure inside the chamber was constant at ±5% atmosphere pressure during the flame propagation within the observation period for flame radius measurement for all conditions (see Fig. AI in Appendix).

A polynomial relationship for the measured flame propagation radius as a function of time was applied to obtain the propagation velocity. As shown in Figs. 5 and 6, although the radius measured by schlieren photography is always larger than that measured by OH radical photography, both methods gave almost the same flame propagation speed.

Furthermore, for all turbulent combustion experiments, the propagation velocities increased with the increase in flame radius, which was the same as that identified in previous pure coal combustion and the pulverized coal/ammonia co-combustion studies [14,15,27]. Additionally, no constant value was observed within the observation range. The increase in the flame propagation velocity with the flame radius is caused by the wrinkling of the flame front by turbulent eddies. As the turbulent flame expands outwardly, the flame becomes more wrinkled and accelerated. In the initial period of flame propagation, only eddies whose size is smaller than the flame size could wrinkle the flame front, but with the development of the flame radius, the flame can be affected by a wider range of turbulence wavelength. Therefore, the flame propagation velocity increases with the increase of the flame radius. The flame propagation velocities at a flame diameter of 0.02090 m (which is equivalent to the integral length scale (L_f) of the turbulent field) were chosen to compare the flame propagation velocities obtained under different conditions. This methodology has been used in many solid and gas combustion studies [14,15,26,27,48–50].

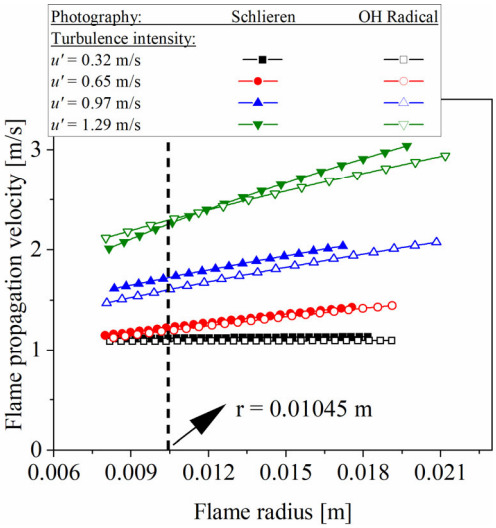

Fig. 6 Fame propagation velocity as a function of flame radius for the 30-μm quasi-monodispersed PMMA particles with a particle cloud concentration of 0.6 kg/m^3.

3.2. Turbulence intensity and particle cloud concentration effects on the turbulent flame propagation of the quasi-monodispersed particle cloud combustion

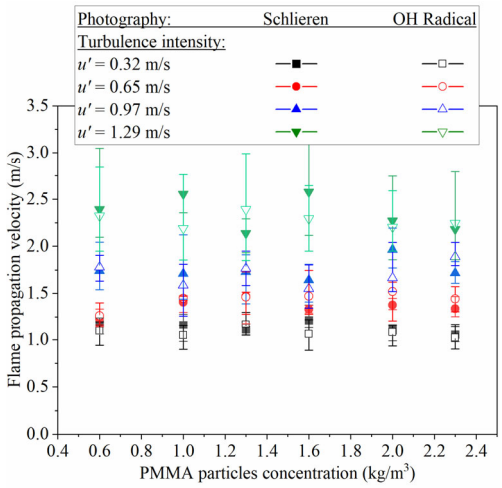

(a) Flame propagation velocity in terms of PMMA particle concentration under different turbulence intensity for the 30-μm quasi-monodispersed PMMA particles

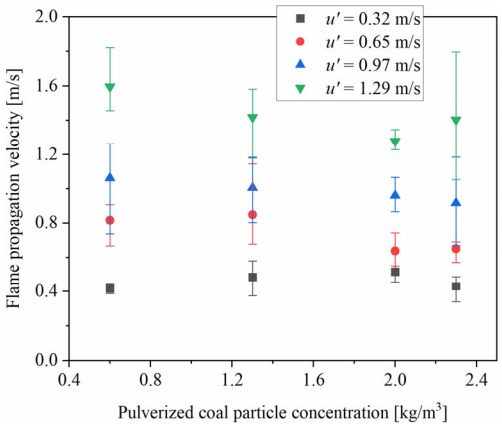

(b) Flame propagation velocity in terms of particle concentration under different turbulence intensity for the polydispersed pulverized coal particles [14]

Fig. 7 Flame propagation velocity as a function of particle concentration for different fuel materials.

Figure 7(a) shows the relationship of the flame propagation velocity as a function of particle concentration for the 30-μm quasi-monodispersed particle clouds. To obtain a clear schlieren image even at a high particle concentration, experiments to clarify the particle concentration effect were conducted with the 30-μm quasi-monodispersed particles. As shown in Fig. 7(a), the turbulent flame propagation velocity of the PMMA particle clouds increased with the increase in turbulence intensity. Two major reasons cause this tendency. First, as the turbulence intensity increases, the turbulence heat and mass transfer can be enhanced. The enhanced turbulence heat and mass transfer can promote the release of the volatile matter. Subsequently, the flame propagation velocity can be increased. Second, the flame surface area can be increased with the increase in turbulence intensity. Consequently, the turbulent flame propagation velocity increased with the increase in turbulence intensity.

Additionally, the PMMA particle cloud concentration had little effect on the turbulent flame propagation velocity. This tendency was also found in the pulverized coal particle cloud combustion, which can be seen in Fig. 7(b) [14]. Therefore, in solid particle cloud turbulent combustion, the particle concentration has a weak effect on the flame propagation velocity. This tendency is different from that in a quiescent environment in which the flame propagation velocity reaches a maximum value for a specific particle concentration [5–8]. In a quiescent condition in which no natural convection or buoyancy effect exists, the particle cloud flame propagation velocity is mainly controlled by the heat conduction between gas and particles and radiation between particles [5]. Therefore, the distance between particles plays a key role in the flame propagation phenomenon. Accordingly, the particle concentration dominates the flame propagation phenomenon in a quiescent condition. However, in the turbulent environment (where the buoyancy effect and natural convection are negligible), the turbulent flame propagation velocity is mainly controlled by the turbulent heat and mass transfer. The radiation between particles has little effect on the turbulent flame propagation velocity. Therefore, particle concentration weakly affects the turbulent flame

propagation velocity. Furthermore, an increase in the turbulent intensity enhances the turbulent heat and mass transfer. Hence, the flame propagation velocity increases with turbulence intensity.

Besides, the PMMA particle cloud flame propagation velocity is larger than that of the pulverized coal particle clouds combustion under the same particle cloud concentration and turbulence intensity because of the differences in the particle size and the fuel materials. First, the average particle size of pulverized coal particle cloud in the past study was 48-μm [14]. On the other hand, the average particle size of the quasi-monodispersed PMMA particle cloud for Fig. 7(a) was 30-μm. Second, for different fuel materials, the composition of decomposed gases and their combustion behavior differ. Coal particles contain volatile matter, residual carbon, and ash. When combustion occurs, the volatile matter burns in the gas phase after devolatilization, while residual carbon in char particles burns heterogeneously and slowly [51]. On the other hand, for the PMMA particles, there is no residual carbon and ash.

However, as shown in Fig. 7(a) and (b), although the value of turbulent flame propagation velocity of coal particle clouds is different from that of PMMA particle clouds under the same condition, the turbulent flame propagation velocity of the PMMA particle clouds shows the same tendency with that of coal particle clouds. For particle clouds, the flame propagation velocity increases with the increase in turbulence intensity, and the particles concentration weakly affects the flame propagation velocity because, for both particle clouds, the flame propagation velocity is mainly controlled by the devolatilization rate of the particles. The heterogeneous combustion of char particles has little effect on the turbulent flame propagation velocity because of its slow combustion process.

3.3. Co-combustion of different size quasi-mono-dispersed particles

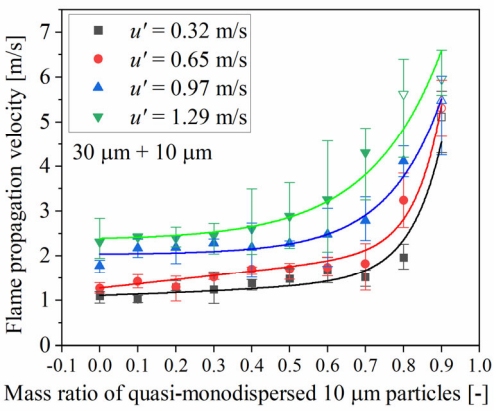

(a) Flame propagation velocity versus the mass ratio of 10-µm quasi-monodispersed particles

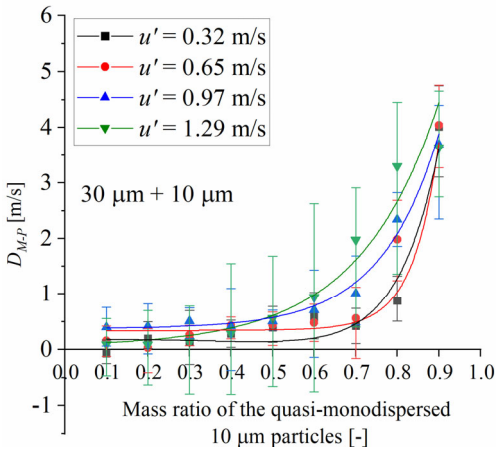

(b) $D_{M\text{-}P}$ versus the mass ratio of 10-µm quasi-monodispersed particles

Fig. 8 Flame propagation tendency of 30-µm quasi-monodispersed particles mixed with 10-µm quasi-monodispersed particles.

First, combustion experiments were conducted by mixing 30-µm quasi-monodispersed particles with 10-µm quasi-monodispersed particles based on the mass ratio under the constant particle cloud concentration of 0.6 kg/m^3. Figure 8(a) shows the flame propagation velocity as a function of mass ratio of 10-µm quasi-monodispersed particles under different turbulence intensities. As shown in Fig. 8, the turbulent flame propagation velocity has a nonlinear relationship with the mass ratio of the small particles (J-shaped curve). The turbulent flame propagation velocity had a very weak increase at relatively low mass ratios of the small particles, while it sharply increased at high mass ratio of the small particles. This trend is called as the nonlinear convex downward relationship. Moreover, the flame propagation velocity increased with the increase in turbulence intensity for all cases. Further, to examine the turbulent flame propagation velocity difference between the combustions of the mixture of quasi-monodispersed particles of different sizes and pure large quasi-mono-dispersed particles, $D_{M\text{-}P}$ was calculated by Eq. (4). Based on the turbulent flame propagation velocity difference between the mixtures that consist of small and large particles and the pure large particles, the increase in the turbulent flame propagation velocity caused by effect of small particles can be estimated under the same turbulence intensity. This methodology is better to obtain the effect of small particles under different turbulence intensities and mixing conditions.

$$D_{M-P} = S_{ws} - S_{wos}, \quad (4)$$

where S_{ws} represents the turbulent flame propagation velocity of the mixed particles with different sizes. S_{wos} represents the turbulent flame propagation velocity of pure large quasi-monodispersed particles combustion, which is in the same turbulent condition as the mixing combustion. For all conditions, first, D_{M-P} slightly increased. Then, there was a sharp D_{M-P} increase under a certain mass ratio of the small particles. As shown in Fig. 8(b), for lower turbulence intensity conditions, which include 0.32 m/s and 0.65 m/s, when the mass ratio of small particles is lower than 0.7, D_{M-P} slightly increases with the increase in the mass ratio of small particles. However, after mass ratio of small particles exceeds 0.7, there is a sharp increase in D_{M-P} with the rise of the mass ratio of small particles. Contrarily, for higher turbulence intensity conditions which include 0.97 m/s and 1.29 m/s, the sharp increase start at a mass ratio (of small particles) of 0.5.

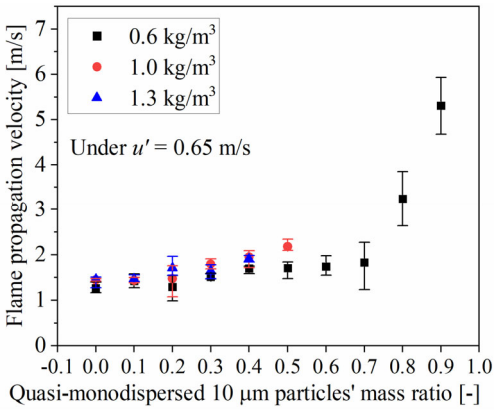

(a) Flame propagation velocity as a function of the mass ratio of 10-μm quasi-monodispersed particles under different particle cloud concentrations

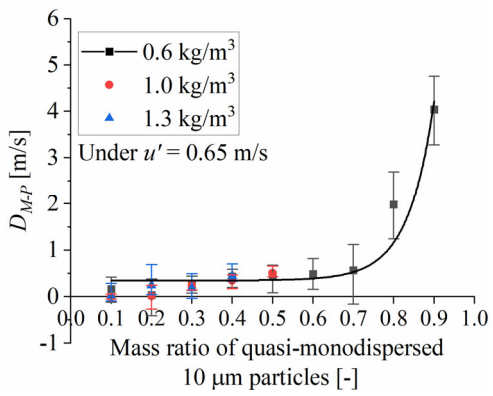

(b) D_{M-P} as a function of the mass ratio of 10-μm quasi-monodispersed particles under different particle cloud concentrations

Fig. 9 Flame propagation tendency versus the small particle mass ratio for the mixture of the 30-μm quasi-monodispersed particles and 10-μm quasi-monodispersed particles under different concentrations of the mixture.

Second, combustion experiments were conducted by changing the mixture's concentration under the same turbulence intensity (u' = 0.65 m/s). Figure 9(a) shows the flame propagation velocity for the mixture of 30-μm quasi-monodispersed particles and 10-μm quasi-monodispersed particles by changing the concentration from 0.6 to 1.3 kg/m^3. Under a particle concentration of 1.0 kg/m^3, schlieren photography and OH radical photography cannot capture the flame propagation images if the 10-μm quasi-monodispersed particles' mass ratio is larger than 0.5. Similarly, for a particle concentration of 1.3 kg/m^3, the two photography methods cannot obtain images if the mass ratio of the 10-μm quasi-monodispersed particles is larger than 0.4. Figure 9(b) shows $D_{M\text{-}P}$ in terms of the mass ratio of 10-μm quasi-monodispersed particles. Under the same turbulence intensity and mass ratio of 10-μm quasi-monodispersed particles, the particle clouds concentration had little effect on $D_{M\text{-}P}$.

Further, combustion experiments were conducted for the mixture of the 30-μm quasi-monodispersed particles and 3-μm quasi-monodispersed particles at a particle concentration of 0.6 kg/m^3. When the mass ratio of small particles was lower than 0.2, if the 10-μm quasi-monodispersed particles were substituted with 3-μm particles in the clouds, the flame propagation velocity remained almost unchanged (see Fig. AJ in Appendix).

Based on the previous findings, to further consider the particle size difference effect in the mixture on the flame propagation phenomenon, combustion experiments were conducted by mixing the quasi-monodispersed 20-μm particles with quasi-monodispersed 10-μm particles. The results are shown in Fig. 10. Through mixing 20-μm particles with 10-μm particles, the sharp increase started at a mass ratio (of small particles) of 0.2. However, it started at around 0.7 for the condition of the mixture of the 30-μm particles with 10-μm particles.

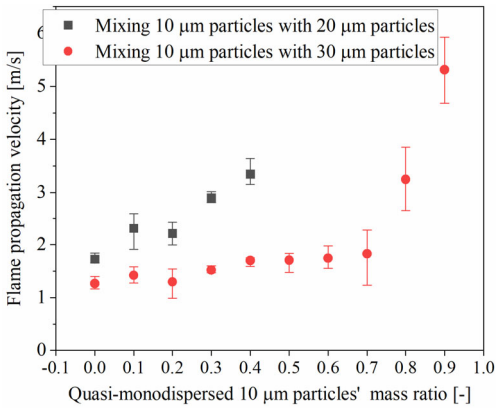

(a) Flame propagation velocity as a function of the mass ratio of 10-μm quasi-monodispersed particles

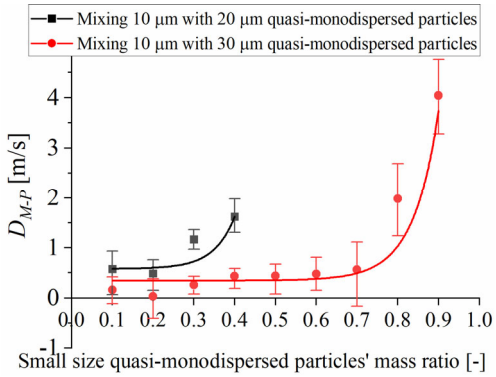

(b) $D_{M\text{-}P}$ as a function of the mass ratio of 10-μm quasi-monodispersed particles

Fig. 10 Flame propagation tendency of the mixture of 20-μm quasi-monodispersed particles and 10-μm quasi-monodispersed particles.

Thus, under the condition of mixing quasi-monodispersed particles with different diameters based on the mass ratio (the primary particle was a large diameter quasi-monodispersed particle), the nonlinear convex downward relationship (J-shaped curve) was found between the mass ratio of the small particles and flame propagation velocity. The turbulent flame propagation velocity first slightly increased with the increase in the small quasi-monodispersed particles' mass ratio. When the small particles' mass ratio increased to a certain point, the flame propagation velocity sharply increased with the rise of the small particles' mass ratio. The flame propagation velocity did not change upon changing the concentration of the particles under the same mixing condition. Moreover, the starting point of the sharp increase of the flame propagation velocity was advanced by increasing the turbulence intensity and decreasing the size of the primary particles (large particles). The mechanism is proposed to explain these tendencies in **Chapter 4**.

3.4. Particle size effect on turbulent flame propagation under quasi-monodispersed particle clouds

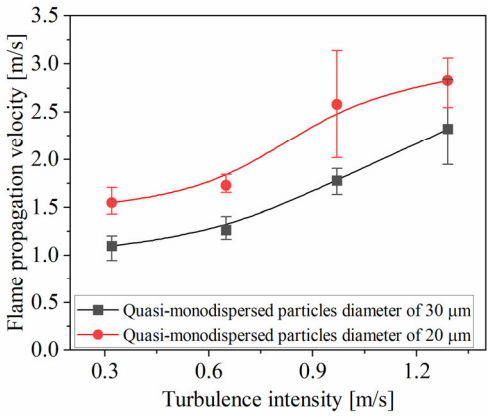

Fig. 11 Turbulent flame propagation velocity versus the turbulence intensity under quasi-monodispersed particles with different diameters.

To clarify the particle size effect on the turbulent flame propagation phenomenon, combustion experiments were conducted using different sizes of quasi-monodispersed particles under a constant particle concentration of 0.6 kg/m^3. As shown in Fig. 11, the flame propagation velocity increases with the decrease in the particle diameter (from 30 μm to 20 μm) under the same turbulence intensity.

However, because of the strong light scattering of the 10-μm quasi-monodispersed particles, the flame propagation images cannot be obtained by schlieren photography and OH radical photography. Therefore, to compare the turbulent flame propagation velocity indirectly, the recorded pressure histories were analyzed. Two key pressure-related values exist to describe the combustion behavior of solid particle clouds in the constant-volume combustion chamber, namely, the maximum pressure and maximum pressure rise rate. The maximum explosion pressure is directly related to the average flame temperature in the vessel. The combustion reaction increases the pressure due to the heat release and temperature rise. Moreover, the maximum pressure rise rate is directly related to the mass burning rate of the fuel. The dust explosion intensity or the maximum rate of the pressure rise is the most direct measurement that best indicates the speed of the deflagration wave [52]. Therefore, the turbulent flame propagation velocity was directly compared with the maximum pressure and maximum pressure rise rate.

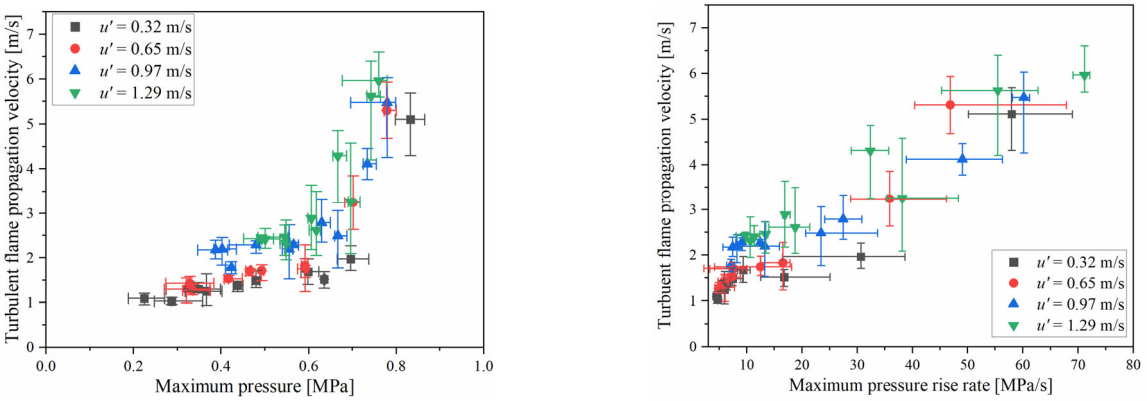

(a) Turbulent flame propagation velocity as a function of the maximum pressure

(b) Turbulent flame propagation velocity as a function of the maximum pressure rise rate

Fig. 12 Turbulent flame propagation velocity as functions of the pressure characteristics for the mixture of 30-μm quasi-monodispersed particles and 10-μm quasi-monodispersed particles under different mass ratios of 10-μm particles and turbulence intensities

Figure 12 shows the turbulent flame propagation velocity as a function of the maximum pressure and the maximum pressure rise rate for the mixture of 30-μm quasi-monodispersed particles and 10-μm quasi-monodispersed particles under different mass ratios of 10-μm particles and turbulence intensities. As shown in Fig. 12(a), under approximately the same turbulent flame propagation velocity, maximum pressure decreases with the increase in the turbulence intensity. This is caused by the turbulent flame–wall interactions. The turbulent vortexes push the flame close to the wall and take the fresh gases away from the wall creating regions of high wall heat flux [53–55]. In high turbulence intensity, the turbulent vortex effect is enhanced because the size range of the turbulent vortex is enlarged. Therefore, for high turbulence intensity, the wall heat flux is higher than that for the low turbulence intensity to increase the heat transfer between the wall and flame.

However, this tendency is not clearly shown in the relation between the turbulent flame propagation velocity and the maximum pressure rise rate because of the non-uniform turbulent flame–wall interaction. Because the turbulent flame is highly deformed in the turbulent environment, the flame partially contacts the wall, whereas part of the flame is still in a flame propagation process. Therefore, the data shows scattering under different turbulence intensities.

Besides, as shown in Fig. 12(b), the turbulent flame propagation velocity increases with the maximum pressure rise rate. The same tendency was found in quasi-monodispersed particle combustion under different particle sizes. Figures 13(a) and (b) show the turbulent flame propagation velocity as functions of the maximum pressure and maximum pressure rise rate, respectively, in quasi-monodispersed particle combustion. Furthermore, the maximum pressure for the 10-μm quasi-monodispersed particles varied in the range 0.8–1.0 MPa, whereas the maximum pressure rise rate varied in the range 70–93 MPa/s under different turbulence intensities. All values of the maximum pressure and the maximum pressure rise rate for 10-μm quasi-monodispersed particles are much larger than the values of plots shown in Fig. 13. Therefore, it is considered that the flame propagation velocity increases with the decrease in the particle diameter from 20 μm to 10 μm.

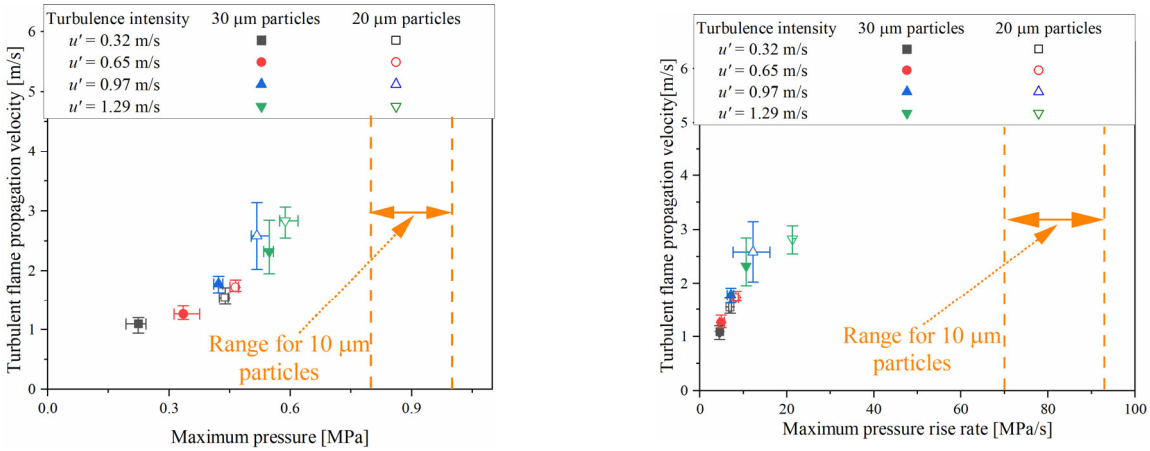

(a) Turbulent flame propagation velocity as a function of the maximum pressure

(b) Turbulent flame propagation velocity as a function of the maximum pressure rise rate

Fig. 13 Turbulent flame propagation velocity as a function of pressure characteristics for the combustion of quasi-monodispersed particles under different particle sizes.

For the quasi-monodispersed particles, as the particle size decreased, the ratio of the heat capacity to the surface area of the individual particle decreased. Hence, the time required to heat the particle decreases with decreasing the particle diameter. Accordingly, the small particles can be decomposed and burned

within a short period. Consequently, the turbulent flame propagation velocity for the quasi-monodispersed particles with a smaller diameter is faster than that with a larger diameter. Therefore, the maximum pressure rise rate increases with the decrease in the particle size.

Notably, the findings above were based on the turbulent flame propagation velocity at a flame diameter of 0.0209 m, which is equivalent to the integral length scale of the turbulent field. To examine the effect of the choice of the flame diameter on the results, the flame propagation velocities at a flame diameter of 0.0300 m, which is the maximum flame diameter to obtain flame propagation velocity data under various conditions, were measured and compared. All findings from flame propagation velocities at a flame diameter of 0.0300 m were consistent with those at a flame diameter of 0.0209 m.

4. Turbulent flame propagation mechanism of the combustion of solid particle clouds under quasi-monodispersed particles and the mixture of quasi-monodispersed particles of different size

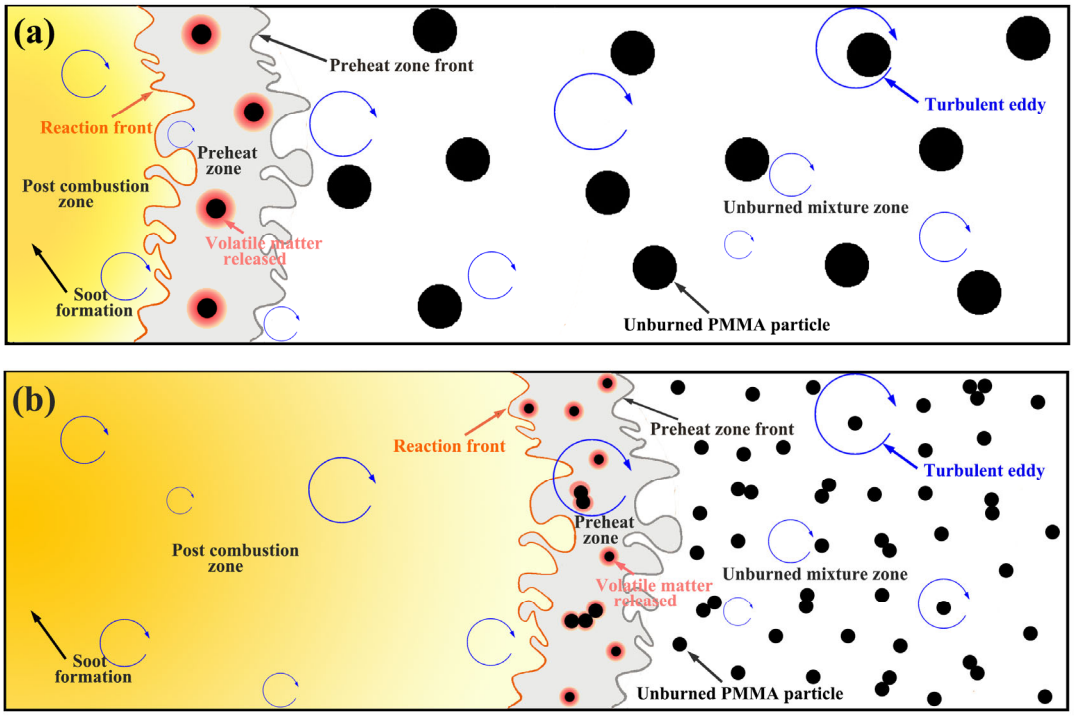

Fig. 14 Turbulent flame propagation mechanism for the combustion of (a) 30-μm quasi-monodispersed particle clouds, (b) 10-μm quasi-monodispersed particle clouds.

The spherical turbulent flame propagation of the PMMA particle cloud combustion can be divided into three zones along the flame propagation direction, including the post-combustion zone, the preheat zone, and the unburned mixture zone. The reaction front, which is detected by OH photography, indicates the combustion reaction starting point. A PMMA particle's combustion follows the sequential process of heat-up, liquefaction, devolatilization or pyrolysis, and combustion. Soot particles are formed by the secondary pyrolysis of volatile matter evolved from PMMA particles. In the preheat zone, PMMA particles just release volatile matter when heated by the turbulent heat transfer from the reaction front. In the PMMA particle cloud turbulent combustion, the turbulent flame propagation velocity is dominated by turbulent heat and mass transfer.

Figures 14(a) and (b) shows the flame propagation mechanisms for the quasi-monodispersed 30-μm particle clouds and the quasi-monodispersed 10-μm particle clouds, respectively. As described in Chapter 3.4, the flame propagation velocity increased with the decrease in the particle diameter from 30 μm to 10 μm. It can be concluded that the specific surface area has an important effect on the flame propagation phenomenon in particle cloud combustion because the small particle, which has a larger specific surface area, can be devolatilized and burned faster.

Further, for the co-combustion of quasi-monodispersed particles with different sizes, we obtained the relationship between the turbulent flame propagation velocity and the mixture's Sauter mean diameter under u' = 0.65 m/s. The Sauter mean diameter, which is generally used to express the mean diameter of the particle cloud, is also called the surface-volume mean diameter. The Sauter mean diameter reflects a collection of spherical objects of different diameters, which is equal to the diameter of identical spherical objects forming an equivalent collection of spheres while both systems have the same total area and total volume [56]. As shown in Fig. 15 (a), for the mixture of the 30-μm particles and 3-μm particles, even though the Sauter mean diameter of the mixture decreased dramatically from 28.3 μm to 10.0 μm, the

turbulent flame propagation was almost the same. Similarly, for the mixture of the 30-μm particles and 10-μm particles, even though the Sauter mean diameter decreased from 28.3 μm to 10.2 μm, the turbulent flame propagation velocity was almost the same. However, for the mixture of the 20-μm and 10-μm particles, even though the Sauter mean diameter decreased slightly from 18.5 μm to 13.4 μm, the turbulent flame propagation velocity largely increased from 1.729 m/s to 3.348 m/s. Besides, the same tendency was found between the turbulent flame propagation velocity and the specific surface area of the mixture (see Fig. AK in Appendix).

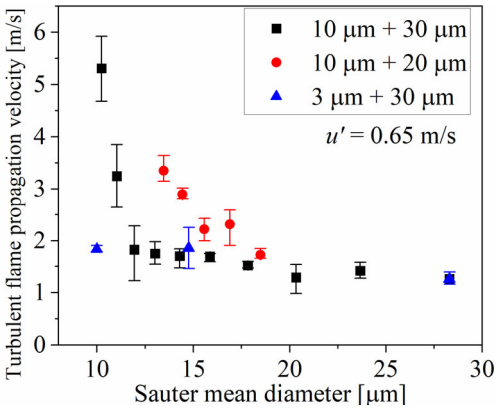

(a) Turbulent flame propagation velocity as a function of the mixture's Sauter mean diameter under different mixing conditions

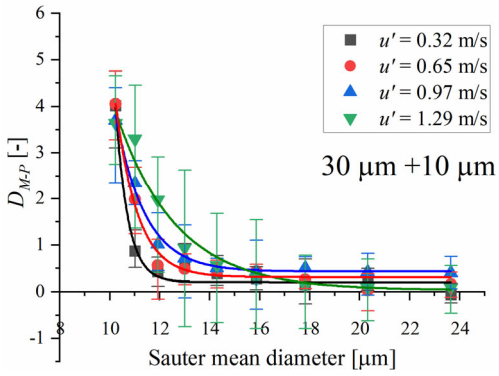

(b) $D_{M\text{-}P}$ as a function of the Sauter mean diameter for the mixture of the 30-μm particles and 10-μm particles

Fig. 15 Turbulent flame propagation characteristics as a function of the Sauter mean diameter under different mixing conditions.

Based on the above discussions, it can be concluded that the flame propagation behavior of mixing different sizes of quasi-monodispersed PMMA particles is not dominated by the total surface area of the particle cloud. Under different mixing conditions, the effective specific surface area and the effective Sauter mean diameter of the mixture are affected by different combinations of particle diameters and mass ratios. Further, for the present research, all experiments were carefully conducted by following the same experimental procedure which was explained in Chapter 2. Therefore, considering the factors affecting

the mixtures' effective specific surface area and the effective Sauter mean diameter (or effective total surface area) in the chamber, the turbulent motion of the particles, and the turbulent particle–particle interactions (agglomeration) in turbulent flow are the dominant factors.

Further, for the mixture of the 30-μm particles and 10-μm particles and the mixture of 20-μm particles and 10-μm particles, under the same mixture's mass and mass ratio of 10-μm particles, the number of 10-μm particles is the same. However, the overall surface area of the 20-μm particles is larger than that of the 30-μm particles. Moreover, the interparticle force is enhanced in the mixture as the large particle size decreases [29,39,57]. This means that the interaction effect should be stronger for the mixture of the 20-μm particles and 10-μm particles. However, based on the experimental data in Fig. 10 and Fig. 15(a), under the same small particles' mass ratio and turbulence intensity, for the mixture of the 30-μm particles and 10-μm particles, the effect of small–large particle interaction is much stronger compared to the mixture of the 20-μm particles and 10-μm particles. By considering the agglomeration effect, this means that most of the small particles are in isolated status for the mixture of 20-μm particles and 10-μm particles. However, for the mixture of the 30-μm and 10-μm particles, most of the small particles are in agglomeration status. Therefore, in turbulent flow, compared to the agglomeration formed by 30-μm with 10-μm particles, the agglomeration formed by the 20-μm with 10-μm particles is easy to be broken up to cause an increase of the mixture's effective specific surface area. Further, under the same turbulence intensity and small particles' mass ratio, even though the effect of small–large particle interaction is stronger for the mixture of 20-μm and 10-μm particles, why the agglomeration formed by them is easy to be broken up? Taking into consideration the agglomeration turbulent break-up mechanism (This mechanism will be explained in detail in the following part), the structure of the agglomeration must be considered (the turbulence effect is the same because the turbulence intensity is the same).

Besides, Fig. 15(b) shows $D_{M\text{-}P}$ as a function of the Sauter mean diameter for the mixture of the 30-μm and 10-μm particles under different turbulence intensities. If do not consider the turbulent effect on the

agglomeration structure, the value of $D_{M\text{-}P}$ should be approximately the same under a certain small particles' mass ratio with different turbulence intensities because the small particles' effect is the same under a certain small particles' mass ratio. However, for lower turbulence intensity conditions, which include 0.32 m/s and 0.65 m/s, the sharp increase starts from the calculated Sauter mean diameter of 12 μm. However, for higher turbulence intensity conditions, which include 0.97 m/s and 1.29 m/s, the sharp increase trend starts from the calculated Sauter mean diameter of 16 μm. Therefore, the small–large particle interaction is different under different turbulence intensity conditions.

To understand the above turbulence flame propagation behavior in the co-combustion of different size quasi-monodispersed particles, we proposed a mechanism based on small–large particle interactions (see Fig. 16). The agglomeration effect on the combustion phenomenon has been studied for many years in the combustion filed [58–60]. Based on previous studies and above discussions, we believe that agglomeration has a dominant effect on the turbulent flame propagation phenomenon under the mixing of particles of different sizes.

After the particles are dispersed into the chamber, they are in motion, caused by the surrounding turbulent gas flow (The Brownian motion and gravitational settling are negligible compared to turbulence-induced motion [61]). The turbulence-induced particle motion can cause collisions between particles [39]. During the process of the collision between the particles, the particles can agglomerate together to form the agglomerate caused by the interparticle force [39,61].

After the particles collide and agglomerate together, they form irregular shapes or fractals [62–67]. The morphology structure of the agglomerates is characterized by the fractal dimension, which also indicates the spatial mass distribution of the particles. Depending on the agglomeration structure, the agglomerate may have a fractal dimension between 1 (straight line) and 3 (compact spherical solid body) [39]. Generally, strong random motions of particles form irregular agglomerates with a small fractal dimension; in contrast, strong centripetal force favors the formation of spherical agglomerates [68].

In the turbulent flow field, the individual agglomerates can interact with turbulent structures, which may cause them to segregate to break through the high shearing of the flow or continue to grow with the enhanced collision rate [68–70]. Besides, the break-up of the agglomerates in turbulent flow is mainly controlled by shear flow induced by turbulent eddies and the fractal dimension of the agglomerate [62,68]. The break-up frequency can be increased by decreasing the fractal dimension of the agglomerate since the agglomeration's mechanical strength greatly increases with the increase in the fractal dimension. Moreover, increasing the turbulence intensity can enhance the turbulent shear force to increase the break-up frequency [68].

The agglomeration effect is enhanced with the decrease in the quasi-monodispersed PMMA particle size from 30-μm to 10-μm since the interparticle force is more significant for the small particle with a small mass [29,39,57]. However, the 10-μm quasi-monodispersed particles have the largest flame propagation velocity. It is considered that, for the 10-μm quasi-monodispersed particles, the effective diameter of the agglomerates is smaller than that of the larger-diameter quasi-monodispersed particles.

Compared to the agglomerates formed by 10-μm particles in quasi-monodispersed 10-μm particles combustion and the agglomerates formed by 10-μm and 20-μm particles in co-combustion of 10-μm and 20-μm quasi-monodispersed particles, the agglomerates formed by the 10-μm with 30-μm particles in co-combustion of 10-μm and 30-μm quasi-monodispersed particles are considered to have a larger fractal dimension. There are two major reasons: First, the single 30-μm particle has a large surface area to adhere small particles. Therefore, the small particles tend to adhere to the surface of the large particles to form the near-spherical-shaped agglomerates. It was confirmed by past studies that the more the dust particles in a dust cloud deviate from monodispersity, the faster the cloud coagulates [29,71]. Second, in the polydispersed particle clouds, the particles in the agglomerate are packed closer than that in the quasi-monodispersed particles since the small particles tend to fill the voids in the agglomerate [72].

Further, the agglomerates which have a small fractal dimension are easy to be broken up by the shear flow. Accordingly, the large agglomerates in 10-μm quasi-monodispersed particle clouds and the mixture of 10-μm and 20-μm quasi-monodispersed particle clouds are easy to be broken up to form isolated particles and small agglomerates.

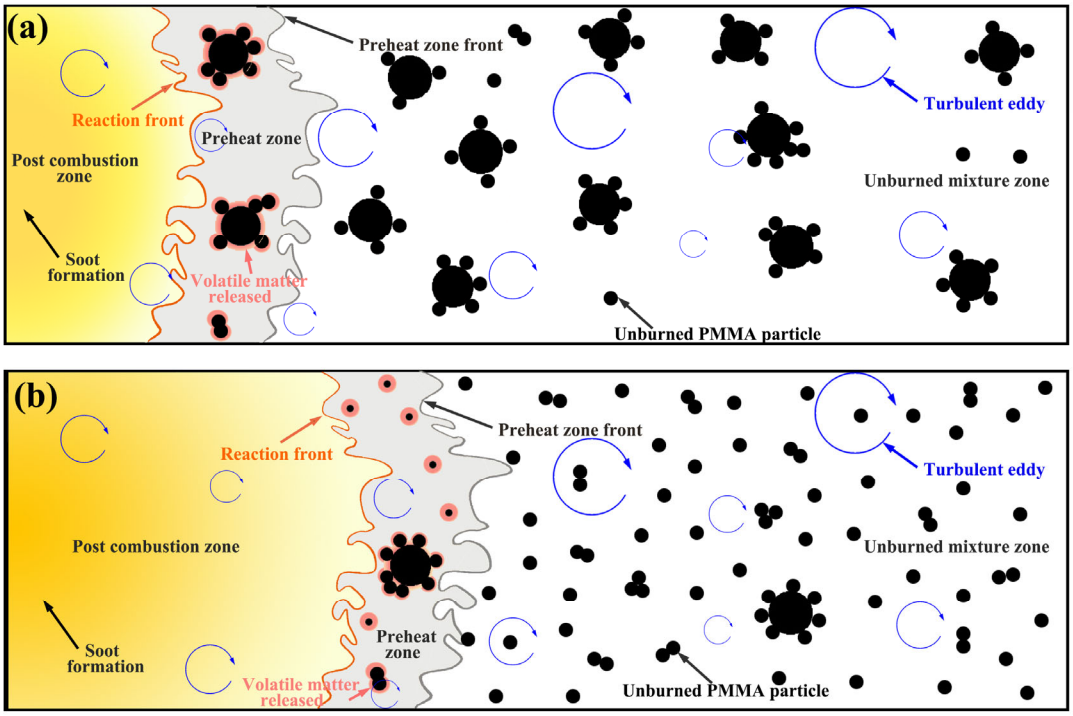

Fig. 16 Proposed turbulent flame propagation mechanism considering polydispersed interparticle interactions; (a) mixture of 30-μm quasi-monodispersed particles and 10-μm quasi-monodispersed particles with a small mass ratio of 10-μm particles, (b) mixture of 30-μm quasi-monodispersed particles and 10-μm quasi-monodispersed particles with a large mass ratio of 10-μm particles.

Figures 16(a) and (b) show the proposed turbulent flame propagation mechanism considering polydispersed interparticle interactions for the mixed 30-μm and 10-μm quasi-monodispersed particles. When the 10-μm quasi-monodispersed particle concentration is low, most of these small particles adhere to the surface of the large particles to form large agglomerates. As elucidated previously, this types of agglomerates with large fractal dimensions are hard to be broken up by the turbulent shear force. Furthermore, the devolatilization rate of these large agglomerates is low because of the small effective specific surface area compared to that of the isolated particles. The small particles which do not adhere to

the large particles in the mixture remain isolated or in the small agglomerate. The isolated small particles or small agglomerates have a large effective specific surface area, which can be devolatilized faster than large agglomerates. The number of isolated small particles or agglomerates increase with the increase in the mass ratio of the small-diameter particles because the increase of mass of the small particles can increase the collision possibility between small particles. However, when the concentration of small particles is low, most of the small particles adhere to the surface of large particles to form large agglomerates. Accordingly, although there are a small amount of isolated small particles or small agglomerates to increase the mixture's effective specific surface area, the overall effective specific surface area of the mixture is mainly controlled by large agglomerates. Therefore, the flame propagation velocity slightly increases when the small particles with a small mass ratio are added under different turbulence intensities. Furthermore, after the mass ratio of small particles reaches a certain value, the overall effective specific surface area of the mixture is controlled by the isolated small particles or small agglomerates. Therefore, the flame propagation velocity abruptly increases as the mass ratio of small particles exceeds a certain value.

Additionally, as the turbulence intensity increases, the starting point of the sharp increase of the flame propagation velocity is advanced. As the turbulence intensity increases, the break-up frequency can be increased because of the strong shear flow induced by turbulent eddies [68]. The intensive break-up events can cause large agglomerates to be separated to form more isolated small particles or small agglomerates. Accordingly, under the same small particle mass ratio, more isolated small particles or small agglomerates are included in the mixture to increase the overall effective specific surface area of the mixture. Finally, the starting point is advanced under high turbulence intensity.

Moreover, the starting point of the sharp increase of flame propagation velocity is advanced under mixing 10-μm quasi-monodispersed particles with 20-μm quasi-monodispersed particles. As elucidated previously, compared to the agglomerates formed by 10-μm and 30-μm particles in the mixture of 10-μm

quasi-monodispersed particles with 30-μm quasi-monodispersed particles, the agglomerates formed by 10-μm and 20-μm in mixture of 10-μm quasi-monodispersed particles with 20-μm quasi-monodispersed particles are considered to have a small fractal dimension. The agglomerates having small fractal dimensions are easy to be broken up by the shear force. Consequently, under the same mass ratio of small quasi-monodispersed particles, a larger number of the isolated small particles or small agglomerates are formed in the mixture of 10-μm quasi-monodispersed particles and 20 μm quasi-monodispersed particles compared to the case of mixing 10 μm and 30 μm particles. Therefore, the starting point of the sharp increase in flame propagation velocity iss advanced.

Besides, the experiments by using the polydispersed particles and quasi-monodispersed particles having approximately the same volume-weighted mean diameter (30 μm) were conducted. The particle size properties of mixtures can be seen in Table AE in Appendix. The particle size distribution data for the polydispersed particles can be seen in Table AF in Appendix. Moreover, the size range of the polydispersed particles varies between 10 μm and 60 μm. The result (which can be seen in Fig. AL in the Appendix) shows that, the turbulent flame propagation velocity of polydispersed particles is slightly larger than (or almost same with) that of the quasi-monodispersed particles. If considering the agglomeration effect on the turbulent flame propagation phenomenon, the small particles with large particles, which have a large particle size difference, will form the agglomerates having a large fractal dimension. However, for the particles which have a small size difference, the agglomerate will have a small fractal dimension. Finally, the overall effective specific surface area of the polydispersed particles is slightly larger than (or almost same with) that of the quasi-monodispersed particles.

5. Conclusions

The effects of the particle cloud concentration and particle size on the turbulent flame propagation of solid particle clouds were studied using the quasi-monodispersed PMMA particle clouds. A simplified

polydispersed particle cloud was formed by mixing two different diameters of the quasi-monodispersed particles to study the turbulent combustion phenomenon associated with small–large particle interactions. The findings can be summarized as follows:

For the combustion of quasi-monodispersed PMMA particle clouds, the flame propagation velocity increases with the increase in the turbulence intensity, and the particle concentration weakly affects the flame propagation velocity. The same tendency has been observed in our previous study for the coal particle cloud combustion [14]. The consistency of the current and previous results suggest that the heterogeneous combustion of char particles weakly affects the turbulent flame propagation velocity of the combustion of solid particle clouds because of its slow combustion process.

Decreasing the quasi-monodispersed PMMA particles' diameter from 30 μm to 10 μm increases the turbulent flame propagation velocity because the small quasi-monodispersed particles have a large specific surface area and can be devolatilized and burned faster.

Under mixing different size quasi-monodispersed particles, the nonlinear convex downward relationship (J-shaped curve) between the turbulent flame propagation velocity and the small particle mass ratio was found. The turbulent flame propagation velocity first slightly increases with the increase in the small particle mass ratio; then the turbulent flame propagation velocity sharply increases after a certain small particle mass ratio. The rise of the turbulence intensity and the decrease in the size of the primary particle (large particle) in the clouds can advance the starting point of sharp increase. The above flame propagation behavior of mixing different size of quasi-monodispersed PMMA particles is not dominated by the total surface area of the particle cloud. The mechanism considering the polydispersed interparticle interaction was suggested to explain above results. In the mixture, the agglomeration between small and large particles forms large agglomerates, which have a lower effective specific surface area than the isolate large particles. The isolated small particles or small agglomerates have a large effective specific surface area. When the concentration of small particles is low, most of the small particles adhere to the surface of

large particles to form large agglomerates and dominate the mixture's overall effective specific surface area. After reaching a certain small particle mass ratio (the starting point of sharp increase), the overall effective specific surface area of the mixture is mainly controlled by isolated small particles or small agglomerates. Additionally, increasing the turbulence intensity can increase the shear force and, in turn, the agglomeration break-up frequency to form more isolated small particles or small agglomerates and furtherly advance the starting point of the sharp increase. Decreasing the primary particle (large particles) size in the mixture can decrease the fractal dimension of agglomerates. Further, agglomerates having a small fractal dimension are easy to be broken up by the shear flow to increase the number of small agglomerates or isolated small particles.

Acknowledgments

This work was partly supported by JSPS KAKENHI Grant Number JP19180646 and JST Sakigake (PRESTO) Grant Number JPMJPR1542. The Scanning Electron microscope experiments were conducted at joint-use facilities in Hokkaido University, supported by "Microscopic Analysis for Nano materials science and Bio science Open Unit (MANBOU)" under MEXT Program for supporting introduction of the new sharing system, Grant Number JPMXS0420100520. The authors thank Mr. K. Ohkubo and Mrs. C. Tsukada for their help in FE-SEM observation. Yu Xia was funded by the Chinese Scholarship Council (Grant no. 201806420020).

References

[1] K. Seshadri, A.L. Berlad, V. Tangirala, The structure of premixed particle-cloud flames, Combust. Flame 89 (1992) 333–342.

[2] M.D. Horton, F.P. Goodson, L.D. Smoot, Characteristics of flat, laminar coal-dust flames, Combust. Flame 28 (1977) 187–195.

[3] O. Fujita, K. Ito, T. Tagashira, Measurement of flame propagation speed of coal dust using a microgravity environment, Heat Transf. Microgravity 269 (1993) 59–66.

[4] H. Kobayashi, N. Ono, Y. Okuyama, T. Niioka, Flame propagation experiment of PMMA particle cloud in a microgravity experiment, Symp. (Int.) Combust. 25 (1994) 1693–1699.

[5] T. Suda, K. Masuko, J. Sato, A. Yamamoto, K. Okazaki, Effect of carbon dioxide on flame propagation of pulverized coal clouds in CO_2/O_2 combustion, Fuel 86 (2007) 2008–2015.

[6] L.D. Smoot, M.D. Horton, G.A. Williams, Propagation of laminar pulverized coal-air flames, Symp. (Int.) Combust. 16 (1977) 375–387.

[7] M. Taniguchi, H. Kobayashi, S. Auhata, Laser ignition and flame propagation of pulverized coal dust clouds, Symp. (Int.) Combust. 26 (1996) 3189–3195.

[8] M. Taniguchi, H. Kobayashi, K. Kiyama, Y. Shimogori, Comparison of flame propagation properties of petroleum coke and coals of different rank, Fuel 88 (2009) 1478–1484.

[9] S.E. Slezak, R.O. Buckius, H. Krier, Evidence of the rich flammability limit for pulverized pittsburgh seam coal-air mixtures, Combust. Flame 63 (1986) 209–215.

[10] H. Hanai, M. Ueki, K. Maruta, H. Kobayashi, S. Hasegawa, T. Niioka, A lean flammability limit of polymethylmethacrylate particle-cloud in microgravity, Combust. Flame 118 (1999) 359–369.

[11] D.R. Ballal, Ignition and flame quenching of quiescent dust clouds of solid fuels., Proc. R. Soc. London, Ser. A Math. Phys. Sci. 369 (1980) 479–500.

[12] J. Jarosinski, J.H. Lee, R. Knystautas, J.D. Crowley, Quenching of dust-air flames, Symp. (Int.) Combust. (1986) 1917–1924.

[13] H. Hanai, H. Kobayashi, T. Niioka, A numerical study of pulsating flame propagation in mixtures of gas and particles, Proc. Combust. Inst. 28 (2000) 815–822.

[14] K. Hadi, R. Ichimura, N. Hashimoto, O. Fujita, Spherical turbulent flame propagation of pulverized coal particle clouds in an O_2/N_2 atmosphere, Proc. Combust. Inst. 37 (2019) 2935–2942.

[15] Y. Xia, K. Hadi, G. Hashimoto, N. Hashimoto, O. Fujita, Effect of ammonia/oxygen/nitrogen equivalence ratio on spherical turbulent flame propagation of pulverized coal/ammonia co-combustion, Proc. Combust. Inst. 38 (2021) 4043–4052.

[16] Y.F. Khalil, Dust cloud combustion characterization of a mixture of $LiBH_4$ destabilized with MgH_2 for reversible H_2 storage in mobile applications, Int. J. Hydrogen Energy 39 (2014) 16347–16361.

[17] R.K. Eckhoff, Understanding dust explosions. The role of powder science and technology, J. Loss Prev. Process Ind. 22 (2009) 105–116.

[18] M. Scheid, A. Geißler, U. Krause, Experiments on the influence of pre-ignition turbulence on vented gas and dust explosions, J. Loss Prev. Process Ind. 19 (2006) 194–199.

[19] A.L. Corcoran, V.K. Hoffmann, E.L. Dreizin, Aluminum particle combustion in turbulent flames, Combust. Flame 160 (2013) 718–724.

[20] C.W. Kauffman, S.R. Srinath, F.I. Tezok, J.A. Nicholls, M. Sichel, Turbulent and accelerating dust flames, Symp. (Int.) Combust. 20 (1985) 1701–1708.

[21] Y. K. Pu, J. Jarosinski, C. S. Tai, C. William Kauffman, M. Sichel, The investigation of the feature of dispersion induced turbulence and its effects on dust explosions in closed vessels, Symp. (Int.) Combust. 22 (1989) 1777–1787.

[22] Y.K. Pu, J. Jarosinski, V.G. Johnson, C.W. Kauffman, Turbulence effects on dust explosions in the 20-liter spherical vessel, Symp. (Int.) Combust. 23 (1991) 843–849.

[23] H. Schneider, C. Proust, Determination of turbulent burning velocities of dust air mixtures with the open tube method, J. Loss Prev. Process Ind. 20 (2007) 470–476.

[24] X.Y. Zhang, J.L. Yu, J.H. Sun, W. Gao, Effects of turbulent intensity on nano-PMMA flame propagation behaviors, J. Loss Prev. Process Ind. 44 (2016) 119–124.

[25] R. Ichimura, K. Hadi, N. Hashimoto, A. Hayakawa, H. Kobayashi, O. Fujita, Extinction limits of an ammonia/air flame propagating in a turbulent field, Fuel 246 (2019) 178–186.

[26] Y. Xia, G. Hashimoto, K. Hadi, N. Hashimoto, A. Hayakawa, H. Kobayashi, O. Fujita, Turbulent burning velocity of ammonia/oxygen/nitrogen premixed flame in O_2-enriched air condition, Fuel 268 (2020) 117383.

[27] K. Hadi, R. Ichimura, G. Hashimoto, Y. Xia, N. Hashimoto, O. Fujita, Effect of fuel ratio of coal on the turbulent flame speed of ammonia/coal particle cloud co-combustion at atmospheric pressure, Proc. Combust. Inst. 38 (2021) 4131–4039.

[28] G. Hashimoto, K. Hadi, Y. Xia, A. Hamid, N. Hashimoto, A. Hayakawa, H. Kobayashi, O. Fujita, Turbulent flame propagation limits of ammonia/methane/air premixed mixture in a constant volume vessel, Proc. Combust. Inst. 38 (2021) 5171–5180.

[29] R.K. Eckhoff, Does the dust explosion risk increase when moving from μm-particle powders to powders of nm-particles?, J. Loss Prev. Process Ind. 25 (2012) 448–459.

[30] Y. Yuzuriha, W. Gao, T. Mogi, R. Dobashi, Effects of particle size distributions on flame propagation behavior through dust clouds of PMMA, J. Loss Prev. Process Ind. 49 (2017) 852–858.

[31] X. Zhang, J. Yu, W. Gao, D. Zhang, J. Sun, S. Guo, R. Dobashi, Effects of particle size distributions on PMMA dust flame propagation behaviors, Powder Technol. 317 (2017) 197–208.

[32] J.L. Chen, R. Dobashi, T. Hirano, Mechanisms of flame propagation through combustible particle clouds, J. Loss Prev. Process Ind. 9 (1996) 225–229.

[33] M. Hertzberg, I.A. Zlochower, Devolatilization wave structures and temperatures for the pyrolysis

of polymethylmethacrylate, ammonium perchlorate, and coal at combustion level heat fluxes, Combust. Flame 84 (1991) 15–37.

[34] Soken Chemical & Engineering Company, 2020. Avaliable at Http://www.soken-ce.co.jp/en/product/fine_particles/mx/.

[35] K. Hadi, Spherical flame propagation behavior of pulverized coal particles and ammonia in a turbulent environment, Hokkaido University Library (2019).

[36] R.A. Gore, C.T. Crowe, Effect of particle size on modulating turbulent intensity, Int. J. Multiph. Flow 15 (1989) 279–285.

[37] M. Mandø, Turbulence modulation by non-spherical particles, Aalborg University (2009).

[38] I. Nezu, R. Azuma, Turbulence characteristics and interaction between particles and fluid in particle-laden open channel flows, J. Hydraul. Eng. 130 (2004) 988–1001.

[39] C.T. Crowe, J. D. Schwarzkopf, M. Sommerfeld, Multiphase flow in droplets and particles, CRC press, Boca Raton, 2011.

[40] S. Balachandar, J.K. Eaton, Turbulent dispersed multiphase flow, Annu. Rev. Fluid Mech. 42 (2010) 111–133.

[41] R. Monchaux, M. Bourgoin, A. Cartellier, Analyzing preferential concentration and clustering of inertial particles in turbulence, Int. J. Multiph. Flow 40 (2012) 1–18.

[42] D. Dandy, Bioanalytical Microfluidics Program, Color State Univ n.d. http://navier.engr.colostate.edu/code/code-2/index.html (accessed 04.23.2021).

[43] J.K. Eaton, J.R. Fessler, Preferential concentration of particles by turbulence, Int. J. Multiph. Flow 20 (1994) 169–209.

[44] K.D. Squires, J.K. Eaton, Preferential concentration of particles by turbulence, Phys. Fluids A. 3 (1991) 1169–1178.

[45] T.S. Yang, S.S. Shy, Two-way interaction between solid particles and homogeneous air turbulence: Particle settling rate and turbulence modification measurements, J. Fluid Mech. 526 (2005) 171–216.

[46] H. Yoshimoto, S. Goto, Self-similar clustering of inertial particles in homogeneous turbulence, J. Fluid Mech. 577 (2007) 275–286.

[47] L.P. Wang, M.R. Maxey, Settling velocity and concentration distribution of heavy particles in homogeneous isotropic turbulence, J. Fluid Mech. 256 (1993) 27–68.

[48] C. Mandilas, M.P. Ormsby, C.G.W. Sheppard, R. Woolley, Effects of hydrogen addition on laminar and turbulent premixed methane and iso-octane–air flames, Proc. Combust. Inst. 31 (2007) 1443–1450.

[49] M. Lawes, M.P. Ormsby, C.G.W. Sheppard, R. Woolley, The turbulent burning velocity of iso-octane/air mixtures, Combust. Flame 159 (2012) 1949–1959.

[50] M. Fairweather, M.P. Ormsby, C.G.W. Sheppard, R. Woolley, Turbulent burning rates of methane and methane-hydrogen mixtures, Combust. Flame. 156 (2009) 780–790.

[51] P. Julien, J. Vickery, S. Goroshin, D.L. Frost, J.M. Bergthorson, Freely-propagating flames in aluminum dust clouds, Combust. Flame 162 (2015) 4241–4253.

[52] R.A. Ogle, Dust Explosion Dynamics, Butterworth-Heinemann, United Kingdom, 2017.

[53] R. Palulli, D. Brouzet, M. Talei, R. Gordon, A numerical study of turbulent flame-wall interaction with reduced chemistry, 22nd Australasian Fluid Mechanics Conference (2020), paper 160. doi: 10.14264/75e9676.

[54] G. Bruneaux, K. Akselvoll, T. Poinsot, J.H. Ferziger, Flame-wall interaction simulation in a turbulent channel flow, Combust. Flame. 107 (1996) 27–36.

[55] T. Poinsot, D. Veynante, Theoretical and numerical combustion, Edwards, Inc.,United States of American, 2015.

[56] P.B. Kowalczuk, J. Drzymala, Physical meaning of the Sauter mean diameter of spherical particulate matter, Part. Sci. Technol. 34 (2016) 645–647.

[57] X. Zhang, J. Yu, X. Yan, Q. Xie, W. Gao, Flame propagation behaviors of nano- and micro-scale PMMA dust explosions, J. Loss Prev. Process Ind. 40 (2016) 101–111.

[58] W. Ao, Z. Fan, L. Liu, Y. An, J. Ren, M. Zhao, P. Liu, L.K.B. Li, Agglomeration and combustion characteristics of solid composite propellants containing aluminum-based alloys, Combust. Flame 220 (2020) 288–297.

[59] H. Ito, O. Fujita, K. Ito, Agglomeration of soot particles in diffusion flames under microgravity, Combust. Flame 99 (1994) 363–370.

[60] L. Xiao, W. Pang, Z. Qin, J. Li, X. Fu, X. Fan, Cluster analysis of Al agglomeration in solid propellant combustion, Combust. Flame 203 (2019) 386–396.

[61] C. A. Ho, M. Sommerfeld, Modelling of micro-particle agglomeration in turbulent flows, Chem. Eng. Sci. 57 (2002) 3073–3084.

[62] D.O. Njobuenwu, M. Fairweather, Large eddy simulation of particle agglomeration with shear breakup in turbulent channel flow, Phys. Fluids 30 (2018).

[63] D. R. Rector, B. C. Bunker, Effect of colloidal aggregation on the sedimentation and rheological properties of tank waste, Pacific Northwest Lab., Richland, WA, USA, 1995.

[64] M. Soos, J. Sefcik, M. Morbidelli, Investigation of aggregation, breakage and restructuring kinetics

of colloidal dispersions in turbulent flows by population balance modeling and static light scattering, Chem. Eng. Sci. 61 (2006) 2349–2363.

[65] Z. Zhou, B. Chu, Light-scattering study on the fractal aggregates of polystyrene spheres: Kinetic and structural approaches, J. Colloid Interface Sci. 143 (1991) 356–365.

[66] G.A. Kelesidis, M.R. Kholghy, J. Zuercher, J. Robertz, M. Allemann, A. Duric, S.E. Pratsinis, Light scattering from nanoparticle agglomerates, Powder Technol. 365 (2020) 52–59.

[67] G.A. Kelesidis, S.E. Pratsinis, Soot light absorption and refractive index during agglomeration and surface growth, Proc. Combust. Inst. 37 (2019) 1177–1184.

[68] X. Deng, R.N. Davé, Breakage of fractal agglomerates, Chem. Eng. Sci. 161 (2017) 117–126.

[69] G. Falkovich, A. Fouxon, M.G. Stepanov, Acceleration of rain initiation by cloud turbulence, Nature 419 (2002) 151–154.

[70] M.W. Reeks, Transport, mixing and agglomeration of particles in turbulent flows, Flow, Turbul. Combust. 92 (2014) 3–25.

[71] H.L. Green, W.R. Lane, Particulate clouds: dusts, smokes and mists. Their physics and physical chemistry and industrial and environmental aspects., London, E. & F. N. Spon, Ltd., 1964.

[72] M. Sommerfeld, S. Stübing, A novel Lagrangian agglomerate structure model, Powder Technol. 319 (2017) 34–52.